PCCP

PAPER

View Article Online
View Journal | View Issue

Cite this: *Phys. Chem. Chem. Phys.*, 2016, **18**, 23407

Electronic properties of highly-active Ag_3AsO_4 photocatalyst and its band gap modulation: an insight from hybrid-density functional calculations†

Pakpoom Reunchan,[a] Adisak Boonchun*[a] and Naoto Umezawa[b]

Received 26th May 2016,
Accepted 29th July 2016

DOI: 10.1039/c6cp03633c

www.rsc.org/pccp

The electronic structures of highly active Ag-based oxide photocatalysts Ag_3AsO_4 and Ag_3PO_4 are studied by hybrid-density functional calculations. It is revealed that Ag_3AsO_4 and Ag_3PO_4 are indirect band gap semiconductors. The Hartree–Fock mixing parameters are fitted for experimental band gaps of Ag_3AsO_4 (1.88 eV) and Ag_3PO_4 (2.43 eV). The smaller electron effective mass and the lower valence band edge of Ag_3AsO_4 are likely to be responsible for the superior photocatalytic oxidation reaction to Ag_3PO_4. The comparable lattice constant and analogous crystal structure between the two materials allow the opportunities of fine-tuning the band gap of $Ag_3As_xP_{1-x}O_4$ using a solid-solution approach. The development of $Ag_3As_xP_{1-x}O_4$ should be promising for the discovery of novel visible-light sensitized photocatalysts.

1 Introduction

Much attention has been paid to photocatalysts based on oxide semiconductors for degrading organic contaminants as well as splitting water into H_2 and O_2. Since the discovery of the TiO_2 photocatalyst, many efforts have been made to reduce its band gap (3.2 eV) because it can only absorb ultraviolet light and utilizes about 5% of solar energy. A widely adopted approach is doping with foreign elements, either cations or anions, for sensitizing TiO_2 under visible light irradiation to increase the conversion efficiency of solar energy.[1] However, doping is often accompanied by the formation of trapping centers of photo-excited carriers and degrades the quantum efficiency; the ratio of the number of photoexcited carriers that actually participate in the photocatalytic reaction to the number of photoexcited carriers that are initially produced by photons. Development and synthesis of visible-light-responsive photocatalysts such as $AgAl_{1-x}Ga_xO_2$,[2] CdS,[3] and $BiVO_4$[4] is another approach to tackle the aforementioned problem. Recently, silver orthophosphate (Ag_3PO_4) was discovered to exhibit extremely high photocatalytic activity for O_2 evolution from water, and its quantum efficiency is nearly 90% under visible light irradiation.[5] This triggered several studies of the development of Ag_3PO_4 in various aspects such as facet engineering,[6] external doping,[7] and combining with other materials such as graphene.[8] More recently, it has been reported that Ag_3AsO_4 exhibits higher photocatalytic activity than Ag_3PO_4 under visible-light irradiation.[9] The narrow band gap of Ag_3AsO_4 (1.60–1.88 eV)[9,10] and the potential of the valence band edge that is sufficiently positive (2.2 eV referenced to normal hydrogen electrode potential, NHE) were attributed to the high oxidation ability of photogenerated holes that participate in decomposing the organic pollutants. A question arises as to why Ag_3AsO_4 exhibits superior oxidation photocatalytic activity to Ag_3PO_4. Efforts have been made to understand the electronic and optical properties as well as the origin of high photocatalytic activity of Ag_3PO_4[11–13] and Ag_3AsO_4 under visible light.[14] Only a recent work reported a comparative theoretical and experimental study of silver oxosalts, including Ag_3PO_4 and Ag_3AsO_4.[10] The origin of the band gap difference and qualitative trends in the photocatalytic activity were discussed based on density functional theory calculations using a generalized gradient approximation (GGA).[10] However, the band offset and the band gap engineering that are the prime keys for enhancing photocatalytic activities have not been discussed elsewhere.

Forming a solid solution of two semiconductors is a common approach toward band-gap engineering of photocatalysts. For example, an oxynitride $(ZnO)_x(GaN)_{1-x}$ is known to split water into H_2 and O_2 under visible light irradiation.[15] A recent study showed that $AgAlO_2$ and $AgGaO_2$ can form solid solutions, and photoabsorption edges and photocatalytic performance of $AgAl_{1-x}Ga_xO_2$ are controlled by its composition ratio.[2]

In this paper, we perform density-functional theory calculations using a screened hybrid-functional, which have been proven to

[a] *Department of Physics, Faculty of Science, Kasetsart University, Bangkok 10900, Thailand. E-mail: fsciasb@ku.ac.th; Tel: +66856692765*

[b] *International Center for Materials Nanoarchitectonics, National Institute for Materials Science (NIMS), 1-1 Namiki, Tsukuba, Ibaraki 305-0044, Japan*

† Electronic supplementary information (ESI) available: Charge distribution of the valence band maximum and conduction band minimum of Ag_3PO_4 and Ag_3AsO_4 and formation enthalpy of $Ag_3As_xP_{1-x}O_4$ solid solutions. See DOI: 10.1039/c6cp03633c

reliably describe the electronic and structural properties of semiconductors.[16] In contrast to the PBE0 hybrid-functional, an appropriate selection of the Hartree–Fock mixing parameter in the screened hybrid-functional allows ones to reproduce the values of experimental band gaps. Fundamental physical and electronic properties of Ag_3AsO_4 and Ag_3PO_4 are investigated and estimated; physical constants are in excellent agreement with the experimental values. The positions of the valence band and conduction band edges of the two materials relative to the vacuum level are obtained by the band alignment approach using the slab models. The results given by density-functional calculations are considerably different from those obtained by the Mulliken electronegativity approach. We also demonstrate that the band-gap engineering from the formation of the solid solution $Ag_3As_xP_{1-x}O_4$ is a promising approach to enhance the performance of a visible-light responsive photocatalyst. To the best of our knowledge, this is the first report on the investigation of the band gap engineering of $Ag_3As_xP_{1-x}O_4$ alloys.

2 Computational methodology

The screened hybrid-functional proposed by Heyd, Scuceria, and Ernzerhof (HSE),[17] as implemented in the VASP code,[18,19] is employed to study the electronic structures of Ag_3AsO_4, Ag_3PO_4 and its alloys $Ag_3As_xP_{1-x}O_4$. The energy cut-off of 520 eV is set for the plane-wave basis set expansion. The valence electron configurations of the projector augmented wave pseudopotentials are $4d^{10}5s^1$ for Ag, $3s^23p^3$ for P, $4s^24p^3$ for As, and $2s^22p^4$ for O. In order to reproduce the experimental band gaps of Ag_3AsO_4 (1.88 eV) and Ag_3PO_4 (2.43 eV), the Hartree–Fock mixing parameter in the HSE approach of 31.5% and 33% was used, respectively. A set of $4 \times 4 \times 4$ grid of Monkhorst–Pack special k-points is used for the Brillouin zone integrations. For the estimation of the band alignment of the two materials, the slab models with layers of non-polar terminated surfaces along the [001] direction containing 80 atoms were employed with the shifted $1 \times 1 \times 1$ grid of Monkhorst–Pack special k-points. The empty region between the slabs is $\sim$30 Å to ensure that they will not interact with each other. All atoms are relaxed until the residual forces are less than 0.02 eV $Å^{-1}$.

3 Results and discussion

Ag_3AsO_4 and Ag_3PO_4 have the cubic structure with space group $P\bar{4}3n$ with 16 atoms in the primitive unit cell. The calculated lattice constants listed in Table 1 are in very good agreement with experimental values. The HSE functional is found to yield lattice constants of both materials closer to the experimental values than those obtained from LDA,[20] PBE, and PBE0[11,14] functionals. The calculated local atomic structure of Ag_3AsO_4 is shown in Fig. 1. The primitive unit cell is composed of PO_4 and AsO_4 tetrahedra. We find that the As–O bonds (1.697 Å) are $\sim$10% longer than the P–O bonds (1.540 Å) in Ag_3PO_4 whereas the tetrahedral angles remain unchanged ($\sim$110°). Bader charge analysis (Table 2) shows that the O atoms draws electrons from

Table 1 Calculated lattice constant a, energy band gaps (E_g) and heat of formation ΔH_f (eV) of Ag_3AsO_4 and Ag_3PO_4 by the HSE functional. The corresponding experimental values are listed in the parentheses

	Ag_3AsO_4	Ag_3PO_4
a (Å)	6.18 (6.12)[21]	6.05 (6.005)[5]
E_g direct (eV)	1.88 (1.88)[10]	2.49 (2.43)[5]
E_g indirect (eV)	1.75 (unknown)	2.35 (2.36)[5]
ΔH_f (eV)	−5.88 (−6.83)	−10.02 (−10.41)[22]

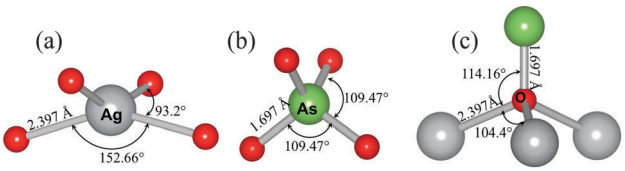

Fig. 1 Local atomic structure of Ag, As and O atoms in Ag_3AsO_4. The calculated values of Ag–O, As–O bond lengths and associated bond angles are also listed.

Table 2 Calculated net charges by Bader analysis for each constituent of Ag_3AsO_4 and Ag_3PO_4

	Ag_3AsO_4	Ag_3PO_4
Ag	+0.685e	+0.704e
As or P	+2.644e	+3.835e
O	−1.175e	−1.487e

the P atom in Ag_3PO_4 nearly 0.31 electrons higher than O atoms in Ag_3AsO_4. By contrast, the Ag–O bond lengths in both Ag_3AsO_4 (2.397 Å) and Ag_3PO_4 (2.396 Å) are nearly identical while the Ag atoms in Ag_3PO_4 are more positive (+0.704e) compared to the Ag atoms in Ag_3AsO_4 (+0.685e). These results indicate that $(Ag^{1+})_3(PO_4)^{3-}$ is more ionic than $(Ag^{1+})_3(AsO_4)^{3-}$. However, our calculated Ag–O bond lengths are different from that calculated by the generalized-gradient approximation (GGA) of 2.344 Å (Ag_3PO_4) and 2.377 Å (Ag_3AsO_4) reported recently.[10]

Fig. 2 shows the calculated band structure of (a) Ag_3AsO_4 and (b) Ag_3PO_4 using the HSE functional. We find that both materials have an indirect band-gap with the valence band maximum (VBM) positions at the M point while the conduction band minimum (CBM) is at the Γ point in the Brillouin zone (see the inset of Fig. 2). It has been reported that Ag_3PO_4 is an indirect band gap semiconductor both experimentally[5] and theoretically.[11–13] The direct transition (Γ–Γ) and the indirect transition (M–Γ) are energetically very close to each other. In Ag_3AsO_4, the experimental band gap ranges from 1.60 eV[9] to 1.88 eV.[10] Jin *et al.*[10] measured the band gaps of a series of silver oxosalts (Ag_3AsO_4, Ag_3CO_4, Ag_3PO_4, Ag_3SO_4 and Ag_3SeO_4) from diffuse reflectance UV spectra. However, transition gaps of a series of silver oxosalts did not verify whether Ag_3AsO_4 and Ag_3PO_4 were direct or indirect band gap materials. We found that the experimental gap of Ag_3PO_4 (2.46 eV) is in good agreement with the previously reported gap of the direct transition of Ag_3PO_4 (2.43 eV).[5] Thus, we adopt the value of 1.88 eV from Jin *et al.*[10] for the experimental direct transition of Ag_3AsO_4 which,

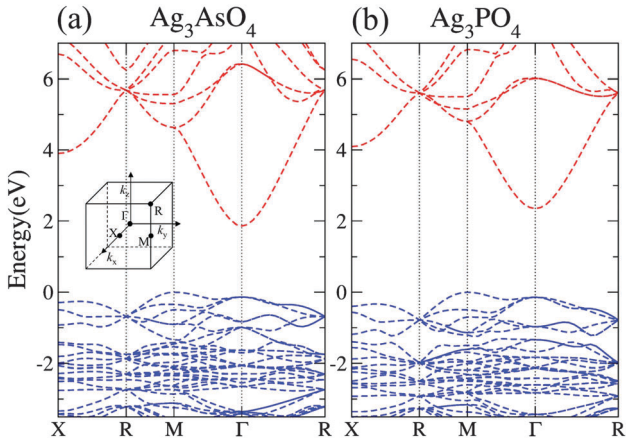

Fig. 2 Calculated band structure of (a) Ag_3AsO_4 and (b) Ag_3PO_4 based on the HSE functional. The Hartree–Fock mixing parameter is set to 31.5% and 33% for Ag_3AsO_4 and Ag_3PO_4, respectively. Inset shows the Brillouin zone and high-symmetry points of the crystal structure.

we found, is reproduced by setting the HF mixing parameter to 31.5%. This scheme yields the indirect band gap of 1.75 eV. The energy difference between the direct and indirect band gaps is ~0.13 eV, which is identical to that of Ag_3PO_4 (Table 1). Note that the PBE0 functional used in ref. 14 yielded the direct band-gap of ~1.80 eV while the GGA functional adopted in ref. 10 predicted Ag_3AsO_4 to be a metal.[10,14] This indicates that GGA or other local functionals cannot reproduce a semiconductor electronic structure even qualitatively for Ag_3AsO_4. In principle, the curvatures of the top of the valence band and bottom of the conduction band determine the hole and electron effective masses, respectively. It can be seen from Fig. 2 that the energy difference between the lowest conduction-band states at Γ and M, $\Delta^{C}_{\Gamma-M}$, is ~2.46 eV for Ag_3PO_4 and ~2.77 eV for Ag_3AsO_4, implying the lower electron effective mass and thus higher electron mobility in Ag_3AsO_4. This statement is evidenced by our calculated electron effective masses of both Ag_3PO_4 and Ag_3AsO_4, which can be expressed as:

$$m^* = \hbar^2 \left(\frac{d^2 E}{dk^2} \right)^{-1} \quad (1)$$

where, E is the band-edge energy near the conduction band minimum as a function of wave-vector k. The electron effective mass is calculated by parabolic fitting the E–k curve within the small region of wave-vector near the CBM. The hole effective mass can be estimated using a similar approach. Table 3 shows the calculated electron and hole effective masses of both materials based on the HSE functional. It was argued that the high electron mobility is an origin of the high photocatalytic activity in Ag_3PO_4.[12] The origin of the lower electron effective mass or in other words the higher dispersion of the conduction band edge in Ag_3AsO_4 can be attributed to the more prominent As character in the conduction band. The density of states for Ag_3PO_4 and Ag_3AsO_4 are shown in Fig. 3a and b. It is clear that the As character in Ag_3AsO_4 is more pronounced than the P character in Ag_3PO_4 at the CBM. This is understood from the bond diagram shown in Fig. 3c, *i.e.*, the shallower As 4p states result in weaker As 4p-O 2p

Table 3 Calculated electron (m_e*) and hole (m_h*) effective mass of Ag_3AsO_4 and Ag_3PO_4 at the Γ point (for electron) and at the M point (for hole) in the Brillouin zone in the units of free-electron mass

	Direction	Ag_3AsO_4	Ag_3PO_4
$m_e^*(\Gamma)$	[100]	0.33	0.42
	[110]	0.33	0.43
	[111]	0.34	0.43
$m_h^*(M)$	[100]	3.38	1.69
	[110]	2.90	1.69
	[111]	1.43	1.39
	[001]	1.03	1.03

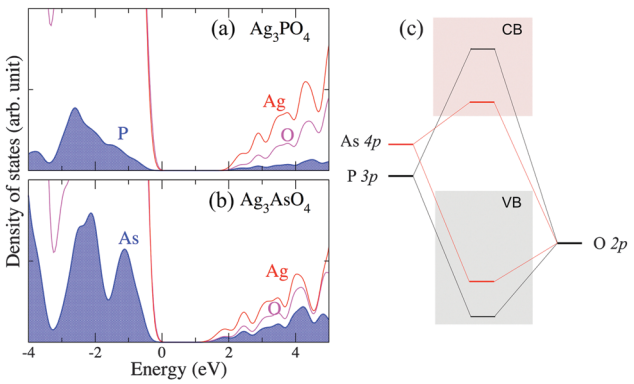

Fig. 3 Projected density of states (PDOS) on each atomic specie in (a) Ag_3PO_4 and (b) Ag_3AsO_4. The shaded areas indicate the PDOS on P and As atoms. The valence band maximum is set at 0 eV and the smearing factor is selectively set for clarity. (c) Schematic diagram for As–O and P–O bonding. Only the interactions between the p states are shown.

bonding–antibonding splitting, allowing the As states coincide with the CBM. The weaker As–O bond leads to the longer As–O bond length of 1.69 Å compared to the P–O bond length of 1.54 Å. Our calculated charge distributions at the CBM show a clear contribution from As atoms in Ag_3AsO_4 while the contribution from P atoms is nearly negligible in Ag_3PO_4 (see the ESI†). It is, therefore, considered that the lower lying As 4p-O 2p antibonding states are readily hybridized with Ag 5s, resulting in the higher dispersion of the CBM and thus lower electron effective mass. Obviously, this also affects the smaller band gap of Ag_3AsO_4. On the other hand, the origin of different hole effective masses of the two materials can be understood as follows. Bader charge analysis (Table 2) shows that the O atoms in Ag_3PO_4 possess more electrons ($-1.487e$) than in Ag_3AsO_4 ($-1.175e$), suggesting a promotion of O 2p-Ag 4d hybridization in Ag_3PO_4. The partial charge distribution of the VBM (M point) shows higher distribution from Ag 4d orbitals in Ag_3PO_4, confirming stronger O 2p-Ag 4d hybridization (see the ESI†). We believe that this is the cause of the higher dispersion of the VBM and smaller hole effective mass of Ag_3PO_4.

In addition to the appropriate band gap values, suitable band edge positions are also vital for a desired visible-light responsive photocatalyst. In order to explain the redox ability in Ag_3AsO_4 and Ag_3PO_4 under visible-light irradiation, the band edge positions referenced to the NHE scale have been calculated. Here, we adopted (1) the Mulliken electronegativity approach and (2) the first-principles band alignment relative to a vacuum level

approach to estimate the position of the band edges. The comparison between the two methods is discussed to analyze the redox ability.

The position of the VB and CB edges according to the Mulliken electronegativity approach[23] can be calculated as $E_{CB} = \chi - E_e - 0.5E_g$ and $E_{VB} = E_{CB} + E_g$, where E_{VB} and E_{CB} are the VB and CB edge potentials, respectively, and E_g is the band gap at Γ. χ is the Mulliken electronegativity of Ag_3AsO_4 and Ag_3PO_4, which is calculated to be about 5.92 eV and 5.96 eV, respectively, based on electron affinities and atomic ionization energies taken from ref. 24. E_e is the energy of free electrons on the hydrogen scale ($\sim$4.5 eV) and E_g is the band gap from our HSE functional approach. The band edge position calculated from Mulliken electronegativity is shown in Fig. 4. The valence band edge potentials (*vs.* NHE) are +2.23 eV for Ag_3AsO_4 and +2.59 eV for Ag_3PO_4 (+2.35 eV for Ag_3AsO_4 and +2.67 eV for Ag_3PO_4 if direct band gap values were used for E_g), which are close to those reported in the recent theoretical works (+2.26 for Ag_3AsO_4[14] and +2.67 eV for Ag_3PO_4[11]). These values of the valence band edge potentials for Ag_3AsO_4 and Ag_3PO_4 are sufficiently positive with respect to the oxidation potential of water (+1.23 eV *vs.* NHE) and suggest both materials are active for photocatalytic O_2 production.

For the band alignment calculations using the slab model, we employed layers of non-polar terminated surfaces along the [001] direction in a vacuum region of $\sim$30 Å. This approach has proven to be practical and widely accepted for the calculations of the band offsets in oxide and nitride semiconductors.[24] The band edge positions relative to the vacuum level are calculated by the following procedures. (1) the energy difference between the vacuum level (V_{vac}) and V_{ae} is calculated to be $\Delta V_{slab} = V_{vac} - V_{ae}$, where V_{ae} is the average electrostatic potential in the bulk region of the slab. (2) The energy difference between the valence band edge positions, E_{VB} and V_{ae}, in the bulk unit cell is determined to be $\Delta V_{bulk} = E_{VB} - V_{ae}$. We thus can estimate the valence band edge position as $E_{VB} = \Delta V_{bulk} - \Delta V_{slab}$. The ionization potentials (the valence band edge positions with respect to the vacuum level) obtained from these procedures for Ag_3AsO_4 and Ag_3PO_4 are depicted in the right panel of Fig. 4, which are −7.20 eV and −7.03 eV, respectively. The higher position of the Ag_3PO_4 valence band edge can be attributed to the higher dispersion of the top of the valence band, consistent with the calculated smaller hole effective mass.

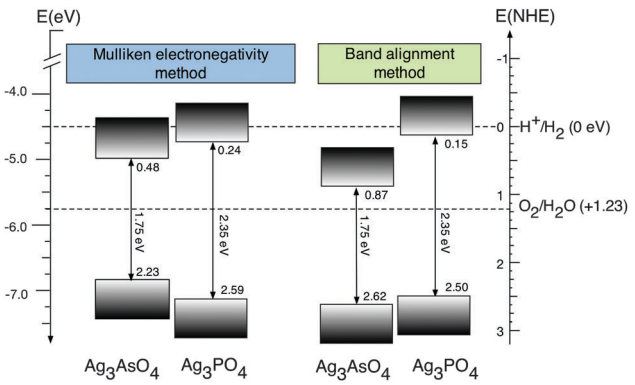

Fig. 4 Calculated valence and conduction band edge positions of Ag_3AsO_4 and Ag_3PO_4 obtained from the Mulliken electronegativity approach (left panel) and the first-principles band alignment approach (right panel) on the absolute energy scale (left vertical axis) and on the natural hydrogen electrode potential scale (right vertical axis). The horizontally aligned numbers are the band edge positions on the NHE scale. The corresponding band gaps (indirect) are also shown.

In order to explain the discrepancy of the band edge positions between the two approaches, we need to understand the concepts beneath the Mulliken method and DFT-based method. The Mulliken method is based on chemical composition and cannot consider the effects of bonding and crystal structure. All polymorphs with the same chemical composition have an equivalent band alignment position. A. Walsh *et al.*[25] showed that in some semiconductors such as ZnO, In_2O_3 GaN and TiO_2, the ionization potential estimated from the Mulliken model is less accurate than that from first-principles calculations; typically its error is in order of 0.5 eV. In our case, the band edge alignment calculations based on density-functional calculations are more advantageous because the Mulliken model fails to describe the bonding of metal d-orbitals.[25] Our calculated band edge positions based on density functional theory predict that Ag_3AsO_4 possesses a lower valence band edge, and thus a stronger oxidation power than Ag_3PO_4. This should be one of the reasons for the observed higher activity for rhodamine degradation on Ag_3AsO_4.[9]

Now, we turn our attention to elucidate the effects of the mixing Ag_3AsO_4 with Ag_3PO_4 to form solid solutions $Ag_3As_xP_{1-x}O_4$ on their band gaps. The modified $Ag_3As_xP_{1-x}O_4$ solid-solutions were calculated using a 32-atom supercell and 16-atom unit cell (which is the primitive cell). As examples, replacing one out of four phosphorus atoms with an arsenic atom in the 32-atom supercell corresponds to the concentration of 25% As ($Ag_3As_{0.25}P_{0.75}O_4$). For the 16-atom unit cell, replacing one phosphorus with an arsenic atom corresponds to the concentration of 50% As ($Ag_3As_{0.50}P_{0.50}O_4$). In this work, we modeled ordered alloys corresponding to the concentration of 0, 25, 50, 75 and 100% As. The lattice parameters and atomic positions were allowed to fully relax. The Hartree–Fock mixing parameter in the HSE approach $Ag_3As_xP_{1-x}O_4$ is linearly interpolated in order to reproduce the correct indirect band gaps for both limiting materials. The variation of the indirect band gap as a function of the composition x in $Ag_3As_xP_{1-x}O_4$ is shown in Fig. 5. We found that the band gap of $Ag_3As_xP_{1-x}O_4$ is nonlinear and can be expressed as[24]

$$E_g(Ag_3As_xP_{1-x}O_4) = (1-x)E_g^{Ag_3PO_4} + xE_g^{Ag_3AsO_4} - bx(1-x) \quad (2)$$

where b is the bowing parameter. In our calculation, we found that the value of the bowing parameter is 0.174. The curvature correction that is characterized by the bowing parameter b in our calculation is rather small, indicating that the band gap of $Ag_3As_xP_{1-x}O_4$ is close to linear. Note that the bowing parameter for the linear equation is equal to zero. Fig. 5 shows the decrease of the band gap when the arsenic concentration increases. Based on our thermodynamic investigation, we also found that the formation of solid solutions is feasible at temperatures of interest. The estimated free energies of mixing yield negative values at

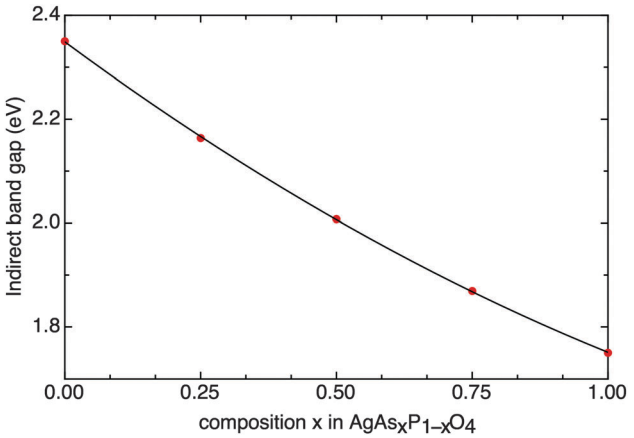

Fig. 5 Variation of the band gap (indirect) of $Ag_3As_xP_{1-x}O_4$ as a function of x as discussed in the text.

temperatures higher than 400 K (see Fig. S3 in the ESI†). The decrease of the band gap with the increase in the As content in $Ag_3As_xP_{1-x}O_4$ is the consequence of the hybridization of multiple states at the CBM. As discussed earlier, the near band-edge hybridizations of As 4p (or P 3p)–O 2p antibonding states with Ag 5s orbitals result in the higher dispersion of the CBM and narrower band gap of Ag_3AsO_4 compared to Ag_3PO_4. Hence, we believe that the different conduction band dispersion in the different As contents is the origin of the band gap variation in $Ag_3As_xP_{1-x}O_4$. There should be other factors that affect the band gap such as the position of the bonding states involving the As–O and P–O hybridization that possibly influences the valence band maximum and the conduction band minimum.

4 Conclusion

In summary, based on the screened hybrid-density functional calculations, we investigated the electronic properties and band offset of Ag_3PO_4 and Ag_3AsO_4. The experimental lattice constants are well reproduced. We found that the origin of the high visible-light photocatalytic activity of Ag_3AsO_4 is attributed not only to its low energy gap, but also its low valence band edge position (more positive on the NHE scale). In addition, we offer an opportunity to modify the band gap of Ag_3AsO_4 through the $Ag_3As_xP_{1-x}O_4$ solid-solutions. Our calculations showed that its band gap can be linearly fine-tuned by varying the As composition. This work not only present the fundamental understanding of the electronic properties of these two important visible-light responsive photocatalysts, but also sheds light on band-gap engineering of silver oxosalts.

Acknowledgements

P. R. and A. B. acknowledge the Kasetsart University Research and Development Institute (KURDI). P. R. and A. B. were supported by Center for Advanced Studies in Industrial Technology, Kasetsart University (NRU-KU) and Faculty of Science, Kasetsart University (grant no. RFG1-4). We wish to thank High-performance computing facilities at the Synchrotron Light Research Institute (SLRI, Thailand) and King Mongkut's University of Technology Thonburi (KMUTT, Thailand) for their hospitality. N. U. would like to thank Y. Tanaka and T. Ohno for useful discussions. This work was partly supported by the Precursory Research for Embryonic Science and Technology (PRESTO) and the Core Research for the Evolutional Science and Technology (CREST) program, the Japan Science and Technology Agency (JST).

References

1 R. Asahi, T. Morikawa, T. Ohwaki, K. Aoki and Y. Taga, *Science*, 2001, **293**, 269–271.
2 S. Ouyang and J. Ye, *J. Am. Chem. Soc.*, 2011, **133**, 7757–7763.
3 M. Matsumura, S. Furukawa, Y. Saho and H. Tsubomura, *J. Phys. Chem.*, 1985, **89**, 1327–1329.
4 A. Kudo, K. Ueda, H. Kato and I. Mikami, *Catal. Lett.*, 1998, **53**, 229–230.
5 Z. Yi, J. Ye, N. Kikugawa, T. Kako, S. Ouyang, H. Stuart-Williams, H. Yang, J. Cao, W. Luo, Z. Li, Y. Liu and R. L. Withers, *Nat. Mater.*, 2010, **9**, 559–564.
6 Y. Bi, S. Ouyang, N. Umezawa, J. Cao and J. Ye, *J. Am. Chem. Soc.*, 2011, **133**, 6490–6492.
7 P. Reunchan and N. Umezawa, *J. Phys. Chem. C*, 2015, **119**, 2284–2289.
8 X. Yang, H. Cui, Y. Li, J. Qin, R. Zhang and H. Tang, *ACS Catal.*, 2013, **3**, 363–369.
9 J. Tang, Y. Liu, H. Li, Z. Tan and D. Li, *Chem. Commun.*, 2013, **49**, 5498–5500.
10 X. Jin, I. Y. Kim, Y. K. Jo, J. L. Bettis, H.-J. Koo, M.-H. Whangbo and S.-J. Hwang, *J. Phys. Chem. C*, 2013, **117**, 26509–26516.
11 J. J. Liu, X. L. Fu, S. F. Chen and Y. F. Zhu, *Appl. Phys. Lett.*, 2011, **99**, 191903.
12 N. Umezawa, O. Shuxin and J. Ye, *Phys. Rev. B: Condens. Matter Mater. Phys.*, 2011, **83**, 035202.
13 P. Reunchan and N. Umezawa, *Phys. Rev. B: Condens. Matter Mater. Phys.*, 2013, **87**, 245205.
14 Y. Gong, H. Yu and X. Quan, *Int. J. Photoenergy*, 2014, **2014**, 5.
15 K. Maeda, K. Teramura, D. Lu, T. Takata, N. Saito, Y. Inoue and K. Domen, *Nature*, 2006, **440**, 295.
16 T. M. Henderson, J. Paier and G. E. Scuseria, *Phys. Status Solidi B*, 2011, **248**, 767–774.
17 J. Heyd, G. Scuseria and M. Ernzerhof, *J. Chem. Phys.*, 2003, **118**, 8207–8215.
18 G. Kresse and J. FurthmÃller, *Phys. Rev. B: Condens. Matter Mater. Phys.*, 1996, **54**, 11169–11186.
19 G. Kresse and J. FurthmÃller, *Comput. Mater. Sci.*, 1996, **6**, 15–50.
20 X. Ma, B. Lu, D. Li, R. Shi, C. Pan and Y. Zhu, *J. Phys. Chem. C*, 2011, **115**, 4680–4687.
21 L. Helmholz and R. Levine, *J. Am. Chem. Soc.*, 1942, **64**, 354–358.
22 E. H. P. Cordfunke and W. Ouweltjes, *Recl. Trav. Chim. Pays-Bas*, 1967, **86**, 93–96.
23 R. S. Mulliken, *J. Chem. Phys.*, 1934, **2**, 782–793.
24 P. G. Moses, M. Miao, Q. Yan and C. G. Van de Walle, *J. Chem. Phys.*, 2011, **134**, 084703.
25 A. Walsh and K. T. Butler, *Acc. Chem. Res.*, 2014, **47**, 364–372.